High fluorescence performance lignin-based carbon quantum dots prepared by supercritical catalytic and solvothermal treatment for target tumor labelling

Siyu Zhao
Guangxi University
Guihua Yue
Guangxi International Zhuang Medicine Hospital
Xiaoli Liu
Guangxi University
Shiru Qin
China University of Mining and Technology
Baosu Wang
China University of Mining and Technology
Peitao Zhao
China University of Mining and Technology
Arthur J. Ragauskas
University of Tennessee
Min Wu
Guangxi University
Xueping Song (sx_ping@gxu.edu.cn)
Guangxi University

Research Article

Keywords: Lignin, catalytic cracking, carbon quantum dots, solvothermal reaction, target labeling tumor cells

Posted Date: December 14th, 2022

DOI: https://doi.org/10.21203/rs.3.rs-2308272/v1

Abstract

The poor fluorescence performance of lignin-based carbon quantum dots (L-CQDs) prepared using the bottom-up method has hindered their development. In this study, a two-step strategy was proposed to efficiently enhance the fluorescence properties of L-CQDs. Lignin was first cracked using an ethanol supercritical/noble metal catalyst; then, the L-CQDs were prepared with the cracked lignin fragments as carbon precursors without adding any modified reagents. Compared with the OL-CQDs prepared by the traditional one-pot hydrothermal method, the L-CQDs-1 prepared from CL-1 containing much low molecular weight compounds, and have photoluminescence (increased from 63 to 975) and excellent up-conversion photoluminescence (enhanced by 16.3 to 963), which significantly enhanced by about 15 times and 60 times, respectively. They can emit bright blue fluorescence under both ultraviolet and near-infrared light irradiation owing to a large amount of surface defects caused by the rich compound composition. When L-CQDs-1 were combined with, and quenched by folic acid (FA), the prepared FA@L-CQDs-1 show the ability to target and label tumor cells. This study opens new avenues for the preparation of L-CQDs with high fluorescence performance using lignocellulosic material without heteroatom additives.

1 Introduction

Since the discovery of carbon quantum dots (CQDs) nearly 20 years ago [1], numerous researchers have explored different raw materials and methods to prepare these highly biocompatible nanofluorescent materials [2–8]. Recently, CQDs have formed a complete system for applications in sensing, medicine, and photocatalysis [7, 9–11]. Using small organic molecules as the carbon source is the main method to prepare high-property CQDs by a "bottom-up" method [12–14]. Because biomass is renewable, widely distributed, and rich in carbon resources, an increasing number of researchers have sought to use biomass materials as carbon sources to prepare CQDs to reduce their preparation cost and maximize the benefits of biomass [15–18]. Lignocellulose accounts for the largest proportion of natural biomass resources, therefore dominating the research in this field [19]. However, compared with the CQDs prepared with small organic molecules, lignocellulose-based CQDs exhibit an uneven size distribution and poor fluorescence performance.

Lignocellulosic biomass is the most abundant natural biopolymer in the world [20–22], which has been widely used in energy storage [23–29], electromagnetic interference shielding [30, 31], oil exploration [32], biosensors [33] and many other fields [34, 35]. Among them, lignin is a macromolecular polymer containing various aromatic structures, and its content is second only to cellulose in lignocellulose resources. However, lignin is usually used as a low-value fuel in the paper industry along with the concentration of black liquor, and its high-value utilization rate is the lowest among the three components of lignocellulose [36, 37]. The realization of high-value utilization of lignin is essential for the valorization of biomass resources. On the other hand, the large number of aromatic structures contained in lignin makes it an ideal raw material for the preparation of CQDs with highly graphitized structures [38]. However, the formation of lignin-based CQDs (L-CQDs), unlike the direct polymerization of small-molecule

carbon sources, primarily includes the depolymerization of lignin macromolecules into small molecules and the repolymerization of small molecules into highly graphitized CQDs through aromatization reactions [16, 39, 40]. Moreover, the lignin aromatic structural units are tightly bound by ether and carbon-carbon bonds, and conventional bottom-up reaction conditions hardly separate the aromatic units. Typically, the depolymerization is accompanies with re-polymerization in the preparation of L-CQDs, resulting in significant randomness and most of the lignin being carbonized before polymerization. These issues in the preparation of L-CQDs significantly hinder the formation of high fluorescence intensity L-CQDs and further limit their application. Improving the fluorescence intensity of L-CQDs is the key to expanding their development. Since the first report of using lignin to synthesize CQDs in 2016 [41], various studies have chosen the same method as small-molecule carbon sources by introducing heteroatomic groups such as N, P, S or metal atoms in the bottom-up reaction process to enhance their fluorescence properties [42–45]. However, the improvement in the fluorescence performance of L-CQDs is still limited, and these introduced groups may restrict their application, especially by easily deteriorating their biocompatibility. Based on the mechanism of lignin-forming CQDs, we speculate that if the lignin is first cracked into low-molecular-weight compounds by an external process and then used as a raw material to prepare CQDs, the fluorescence properties of L-CQDs will be improved. The high fluorescence properties of L-CQDs prepared using a single lignin as the carbon source without the addition of modification reagents will also result in better biocompatibility than those prepared by doping heteroatomic groups or metal atoms, expanding their application value in biomedicine.

In this study, drawing on the principle of traditional supercritical catalytic cracking of lignin to produce bio-oil, we used Pd/C as a catalyst to fragment lignin macromolecules to obtain excellent carbon precursors for the preparation of CQDs with high fluorescence characteristics. Because the vapor pressure of ethanol at 260°C easily causes the catalytic reaction to reach a supercritical state to intensify the cleavage of lignin, ethanol can be converted into acetaldehyde and further produce H_2 [46]. H_2 is introduced to rupture the plentiful β-O-4 bonds in lignin, forming phenolic hydroxyl at the broken end of the ether bond and breaking lignin macromolecules [47, 48]. Ethanol was used as a solvent in the Pd/C catalytic reaction. The effects of different catalytic and critical conditions on the composition and molecular weight of the cracked lignin products were explored. Thereafter, L-CQDs were prepared using the cracked lignin products as the raw material. Based on the chemical, optical, and topological properties of L-CQDs, the influence of hydrogenolysis conditions and catalyst addition on their properties was discussed, and the optimal catalytic cracking process was determined. Finally, the ability of the L-CQDs to target tumor cells was verified by binding L-CQDs to the targeting agent, folic acid. This study provides guidance for the preparation of high-performance CQDs using biomass resources and broadens their applications.

2 Experimental Section

2.1 Materials

Alkali lignin (powder) and palladium carbon (Pd/C) catalysts were purchased from Sigma-Aldrich Co., Ltd. (USA). Ethanol (99.7%), quinine sulfate, dimethyl sulfoxide (DMSO), and folic acid (FA, for cell and insect cell cultures) were purchased from Aladdin Biochemical Technology Co., Ltd. (Shanghai, China). Fetal bovine serum (FBS), 1640 medium, MEM, and trypsin were purchased from Biological Industries Co., Ltd. (Israel). All reagents were used as received. Ultrapure water was obtained using a Milli-Q ultrapure water purification system (Merck KGaA, Germany).

2.2 Supercritical/non-critical catalytic cracking of lignin

4.8 g of alkali lignin, 0.48 g of the Pd/C catalyst and 240 mL of absolute ethanol were added to the quartz liner of a 500 mL high-pressure reactor. The quartz liner was then quickly placed into the reactor, closed, and stirred (100 rpm). The reactor was heated to 260°C and maintained at that temperature for 8 h. When the reaction time was reached, a cooling coil was used to stop the reaction, and when the temperature dropped to approximately 30°C, the reactor was opened. After all reaction products were removed, 50 mL of ethanol was used to wash the reaction kettle, and the washing solution was mixed with the products. Finally, the products were filtered using suction filtration with a 0.45-μm microporous membrane, and the cracked lignin (CL) sample was denoted as CL-1. Three groups of control samples were prepared by changing the reaction conditions, namely CL-2, CL-3, and CL-4, respectively. The preparation conditions for CL-2, CL-3, and CL-4 were as follows:

CL-2: The reaction conditions were the same as those for CL-1, but without the addition of the Pd/C catalyst.

CL-3: The reaction temperature was 220°C. The remainder of the operation was the same as that of CL-1.

CL-4: The reaction temperature was set to 220°C and no Pd/C catalyst was added.

The solid products were repeatedly washed with ethanol and dried, and the CL conversion rate was calculated as follows:

$$Conversion\,(\%) = \left(1 - \frac{m_{solidproduct} - m_{Pd/Ccatalyst}}{m_{lignin}}\right) \times 100\%$$

1

2.3 Preparation of L-CQDs with the solvothermal method

CL (30 mL) was added to a 50 mL PTFE-lined reactor, and then heated to 180°C in an oven and maintained at that temperature for 12 h. After this instant, the reaction was terminated by quickly flushing the reactor shell with ice water. Thereafter, the solid particles were removed via filtration through a 0.22-μm microporous membrane, and the resulting liquid was dialyzed in ultrapure water for 48 h with a dialysis bag (MWCO = 500 Da) to remove incomplete small molecules. Ultra-pure water was changed every 6 h. Finally, the excess solvent was removed using a parallel concentrator, and the solid product was obtained by freeze-drying and named L-CQDs. The L-CQDs prepared using the four CL types were

named L-CQDs-1, L-CQDs-2, L-CQDs-3, and L-CQDs-4, respectively. Unlike our previous studies [40, 45], the prepared L-CQDs were in the form of a paste rather than a powder. The preparation process of L-CQDs is shown in Scheme 1. In addition, 0.1 g of alkali lignin and 30 mL of deionized water were used as solvents to prepare traditional hydrothermal lignin-based CQDs under the same experimental conditions described above, which were denoted as OL-CQDs.

2.4 Quantum yield

The quantum yields (QYs) of the L-CQDs were calculated using quinine sulfate (dissolved in 0.05 mol/L sulfuric acid; QY = 54%) as a reference. The QY of the L-CQDs were calculated at the optimal excitation wavelength for each sample using the following formula:

$$\mathbf{QY} = \mathbf{QY}_{\mathbf{qs}} \bullet \frac{\mathbf{S}}{\mathbf{S}_{\mathbf{qs}}} \bullet \frac{\mathbf{A}_{\mathbf{qs}}}{\mathbf{A}} \bullet \frac{\square^2}{\square^2{}_{\mathbf{qs}}}$$

2

,

where QY is the quantum yield of the L-CQDs, qs is the quinine sulfate reference solution, S is the integral area of the fluorescence peak in the photoluminescence (PL) spectra of the L-CQDs, A is the absorbance of the L-CQDs at the excitation wavelength, and represents the refractive index of the solution.

2.5 Characterization of CL and CQDs

The relative molecular weight and polydispersity (PDI) of the CL samples under different cracking conditions were measured using gel permeation chromatography (GPC; Agilent PL-GPC50, USA) with DMSO as the mobile phase. The compositions of the CL samples were tested using gas chromatography-mass spectrometry (GC-MS; Agilent 7890A GC-5975C MS, USA) with a HP-5MS column. The CL was first condensed to one-fifth of its original volume and then tested by GC-MS. The GC-MS conditions were as follows: the split ratio was 1:50, the helium flow rate was 1.8 mL/min, the injection volume was set at 1 μL, the injection temperature was set at 280°C, and the column temperature was maintained at 60°C for 2 min, then heated to 250°C at a heating rate of 10°C/min, and maintained for another 5 min.

An ultraviolet-visible (UV-vis) spectrophotometer (Hitachi u-4100 UV-vis, Japan) was used to obtain UV-vis absorption spectra of the CQDs. The fluoroluminescence (FL) of the CQDs was measured using a fluorescence spectrophotometer (RF-5301PC, Hitachi, Japan). During the FL measurement, the slit widths of the excitation and emission lights were both 5 nm, and ordinal-valued PL spectra were used to quantify the fluorescence intensity. A Fourier transform infrared (FTIR; Bruker TENSOR II, Germany) spectrometer operated in attenuated total reflectance (ATR) mode was used to elucidate the chemical structure of the L-CQDs. X-ray photoelectron spectroscopy (XPS; Thermo Fisher ScientificTM K-alpha+, USA) was used to measure the carbon and oxygen contents, as well as the functional group compositions on the surfaces of the CQDs. The full-scan XPS spectra were recorded first, followed by the narrow-scan C 1*s* and O 1*s* spectra. The L-CQD microstructure was observed by transmission electron microscopy (TEM; FEI TECNAI

G2 F30, USA) at an acceleration voltage of 300 kV. The three-dimensional (3D) morphology of the L-CQDs was observed using atomic force microscopy (AFM; Bruker Dimension Icon, Germany).

2.6 Cell experiments of L-CQDs

2.6.1 Cytotoxicity and cell imaging

HepG2 and L02 cells in the logarithmic growth phase were collected, and the cells were counted and seeded in laser confocal dishes at 4×10^3 cells/well containing different media (MEM medium with 10% FBS for HepG2 cells and 1640 medium with 20% FBS for L02 cells). L-CQDs-1 and OL-CQDs were separately dissolved in the medium at a concentration of 1 mg/mL. The cells were then incubated for 24 h in a constant-temperature incubator at 37°C and 5% CO_2. Finally, cytotoxicity was tested using the CKK-8 method, and the images of the two cells were captured using a laser scanning confocal microscope (LSCM) at excitation wavelengths of 405 nm and 635 nm.

2.6.2 Preparation of FA@L-CQDs-1 and its targeted recognition to cancer cells

40 µL of 0.1 mol/mL FA solution was added to 4 mL of 1 mg/mL L-CQDs-1 and mixed well using a vortex shaker, which was denoted as FA@L-CQDs-1. At this instant, the fluorescence of the solution was significantly quenched. HepG2 and L02 cells in the logarithmic growth stage were collected, and after cell counting, the cells were seeded in laser confocal dishes at 4×10^3 cells/well containing different media (MEM medium with 10% FBS for HepG2 cells and 1640 medium with 20% FBS for L02 cells). The FA@L-CQDs-1 solution was added dropwise to the cells and incubated for 24 h at 37°C in an incubator containing 5% CO_2. After incubation, the cytotoxicity was tested using the CKK-8 method, and the images of the two cells were taken at excitation wavelengths of 405 and 635 nm using an LSCM.

2.7 Animal in-vivo imaging experiments

First, several nude mice were adaptively fed for a week. HeLa cells in the logarithmic growth phase were collected, and the cell concentration was adjusted to 2×107 cells/mL. HeLa cells (100 µL) were injected into the right subcutaneous tumor implantation site of nude mice. A tumor model was established when the tumor grew to a volume of 100 mm^2. 100 µL of the FA@L-CQDs-1 solution was injected into the tail vein of nude mice. A NightOwl LB 983 3D small-animal imaging system was used for in vivo fluorescence imaging. The observation time points included 0, 0.5, 2, 4, 12, and 24 h after injection. At the end of the observation period, the mice were euthanized, the major organs (heart, liver, lung, kidney, tumor, and spleen) were removed, and their fluorescence images were acquired using the same 3D small animal imaging system. Simultaneously, another nude mouse was fed under the same injection conditions to verify the toxicity of FA@L-CQDs-1.

3 Result And Discussion

3.1 Properties of CL

In this study, the alkali lignin primarily consisted of a guaiacyl-based propane structures as determined by the analysis of by FTIR (**Fig. S1**), 1H- and 13C-NMR analysis (**Fig. S2a, b**). **Fig. S3a-d** shows the temperature-pressure-time curves of the four types of cracked lignin (CL) in the preparation process. With ethanol as the solvent, both CL-1 and CL-2 reached the supercritical state at 260°C, whereas CL-3 and CL-4 did not reach the critical state at 220°C. The conversion rates of lignin for CL-1, CL-2, CL-3, and CL-4 treatments were 64.5%, 62.3%, 58.6%, and 56.7%, respectively. All CL were stably dispersed in ethanol. To investigate the effects of different cracking conditions on the properties of lignin, the relative molecular weight and compound composition of the four types of CL were tested by GPC and GC-MS. As shown in the GPC results in Table 1, the four different cracking conditions reduced the molecular weight of lignin, among which the Mn value of CL-1 decreased most significantly, from 3110 of the original lignin to 1145. The molecular weight of CL increased gradually from CL-1 to CL-4, indicating that both supercritical reaction conditions and noble metal catalysts can significantly promote lignin cracking. Moreover, under the same non-critical conditions, the samples (CL-3) with Pd/C catalysts has lower Mn and Mw values than those of CL-4. Based on the above results, the effects of supercritical conditions and noble metal catalysts on lignin cleavage are synergistic. In addition, the Mn and Mw values of CL-2 are lower than those of CL-4, indicating that supercritical reaction conditions are more conducive to reducing the molecular weight of lignin than noble metal catalysts. Compared with the original alkali lignin, the PDI values of the four kinds of lignin increased to different degrees, primarily because the cracking process reduced the uniformity of the lignin molecular weight. By the photos of the four CL samples under sunlight (**Fig. S4a-d**), it is found that CL-1 and CL-2 are liquid oils, while CL-3 and CL-4 remain powdered, further suggesting that CL-1 and CL-2 have lower molecular weights after the supercritical reaction.

Table 2 shows the composition of the low-molecular-weight compounds in the four CL samples. Figure 1 and **Fig. S5a-c** show the total ion current (TIC) spectra of the CL samples tested using GC-MS. It can be seen from these results that phenolic monomers with G-type structure such as phenol, 2-methoxy-, creosol, 4-ethyl-2-methoxy- are the main components of the cracked lignin. The contents of these monomers in CL-2, CL-3, and CL-4 are greater than 90%, and their contents in CL-1 were approximately 80%. However, a richer composition of compounds is detected in CL-1 than other samples, including a greater variety of aromatic phenols, dimers, and branched compounds from the further cleavage of phenolics. CL-2 has a lower compound composition than CL-1; however, it is still more abundant than CL-3 and CL-4. These results further confirm that both supercritical reaction conditions and noble metal catalysts can promote lignin cracking. The main low-molecular-weight compounds in the CL samples are also shown in Fig. 1.

Table 1
GPC results of cracked lignin.

Samples	Mn	Mw	PDI
Original lignin	3110	13675	2.29
CL-1	1145	2783	3.88
CL-2	1333	9129	2.89
CL-3	1818	8146	3.75
CL-4	2173	14840	3.53

Table 2
GC-MS results of cracked lignin.

Numbers	Retention time (min)	Compounds	Matching rate (%)	Quantify (%)			
				CL-1	CL-2	CL-3	CL-4
1	4.12	Butane, 1,1-diethoxy-	59	5.10	-	-	-
2	4.60	Propanamide, 2-hydroxy-	45	0.04	-	-	-
3	4.76	Butane, 1-methoxy-2-methyl-	47	0.54	-	-	-
4	4.89	Methyl propyl phthalate	12	-	-	-	2.38
5	4.97	Butane, 1-methoxy-	38	-	0.13	-	-
6	5.43	Ethanol, 2-nitro-	38	0.27	-	-	-
7	5.51	Butanoic acid, 4-methoxy-	45	-	0.07	-	-
8	5.84	Propanamide, 2-hydroxy-	53	0.18	-	-	-
9	5.85	2-Propanol, 1,1'-oxybis-	43	-	0.67	-	-
10	6.35	2-(Ethylsulfonyl)ethanol	40	2.31	-	-	-
11	7.29	Phenol, 2-methoxy-	96	54.02	79.68	72.18	78.53
12	8.44	1,2-Benzenediol, 4-methyl-	42	-	0.29	-	-
13	9.03	Creosol	92	11.40	8.86	8.45	5.87
14	9.50	1,3-Benzenediol, 4,5-dimethyl-	64	4.74	-	-	-
15	9.52	Benzene, 1,4-dimethoxy-	46	-	0.86	-	-
16	10.11	Phenol, 4-ethyl-2-methoxy-	87	12.83	6.99	19.38	13.25
17	10.92	O-Methoxy-alpha-methylbenzyl alcohol	46	0.66	-	-	-
18	15.55	1-Propyne, 1-(methylthio)-	38	0.13	-	-	-
19	15.80	2-((2-Ethylbutoxy) carbonyl) benzoic acid	38	0.55	-	-	-
20	16.09	3-Hydroxy-2-pyridin-3-yl-propenal	38	0.43	-	-	-
21	16.22	2H-Pyran-5-carboxamide, 2-oxo-N-(3-chlorophenyl)-	43	0.07	-	-	-
22	16.36	Sydnone, 3-(phenylmethyl)-	53	0.24	-	-	-

Numbers	Retention time (min)	Compounds	Matching rate (%)	Quantify (%)			
				CL-1	CL-2	CL-3	CL-4
23	16.74	Diethyl Phthalate	94	4.80	-	-	-
24	18.47	5-Chloro-2-methyl-3(2H)-isothiazolone	30	0.03	-	-	-
25	19.36	4-Hydroxy-9-fluorenone	70	0.13	-	-	-
26	19.63	Roxarsone	25	0.21	-	-	-
27	20.22	Benzenamine, 4-(4-chloro-1H-pyrazol-1-yl)-	25	0.13	-	-	-
28	21.17	1H-Pyrazole-1-acetamide, N-(2-furanylmethyl)-4-iodo-	25	0.34	-	-	-
29	21.42	Bicyclo[2.2.2]oct-7-ene-2,5-dicarboxylic acid, dimethyl ester	32	0.10	-	-	-
30	21.56	5-Nitrothiophene-2-carboxaldehyde picolinoylhydrazone	40	0.06	-	-	-
31	22.73	Bis(2-ethylhexyl) phthalate	53	0.19	-	-	-
32	23.78	Benzenemethanol, 4-chloro-alpha-methyl-	27	0.15	-	-	-
33	24.79	Tricyclo[4.2.2.0(2,5)]dec-9-ene-7,8-dicarboxylic anhydride, 3-cyano-	64	0.06	-	-	-
34	25.51	Fumaric acid, butyl 4-octyl ester	33	0.18	-	-	-
35	25.84	Thiophene-2-carboxylic acid, 5-formyl-	43	0.09	-	-	-

3.2 Optical properties of L-CQDs

Photographs of the four L-CQDs and OL-CQDs under sunlight and 365-nm UV light are shown in Fig. 2a, b. At a concentration of 1 mg/mL, the OL-CQDs show a brown color under sunlight, whereas the four types of L-CQDs are light yellow or transparent. Under irradiation with 365-nm UV light, the OL-CQDs indicate weak green fluorescence, while the four types of L-CQDs exhibit bright blue or blue-green fluorescence, among which L-CQDs-1 had the highest brightness. The above phenomena indicate that the preparation of L-CQDs using cracked lignin as a precursor by the solvothermal method can effectively improve the fluorescence performance compared to the traditional hydrothermal method using original lignin as a precursor. The UV-vis spectra in Fig. 2c show that all L-CQDs exhibited strong absorption in the

range of 200–400 nm. A buffer appeared near 230 nm owing to the n-n * transition in the aromatic ring, and a strong absorption peak appeared near 280 nm, indicating that n-n *, n-π*, and π-π* transitions occurred in all L-CQDs; thus, all L-CQDs contain C = O functional groups such as carbonyl, carboxyl, or aldehyde groups [49].

The fluorescence properties of all the L-CQDs were measured using a fluorescence spectrophotometer (Fig. 2d-k and Table 3). From Fig. 2d-k, the optimal excitation wavelengths of L-CQDs-1, L-CQDs-2, L-CQDs-3, and L-CQDs-4 are 340, 320, 310, and 320 nm, their corresponding emission wavelengths are 415, 428, 380, and 386 nm, and their fluorescence intensities are 975, 986, 963, and 1143, respectively. At each sample's optimal excitation wavelength, the fluorescence intensities were greatly improved compared with those of the OL-CQDs (63, **Fig. S6a, b**). L-CQDs-4 have the highest fluorescence intensity (1143) among these L-CQDs; however, according to the 3D fluorescence spectra, the optimal emission wavelengths of L-CQDs-3 and L-CQDs-4 are located near 380 nm, which is at the edge of ultraviolet light, so they cannot be effectively recognized by the human eye. The fluorescence intensities of L-CQDs-2, L-CQDs-3, and L-CQDs-4 were not as strong as that of L-CQDs-1 under irradiation with 360–370 nm UV light. As shown in Fig. 2b, L-CQD-1 exhibit the highest visible fluorescence intensity (975) in all L-CQDs, and this value is much higher than that of L-CQDs prepared by the sodium borohydride reduction method (693) and ethylenediamine hydrothermal method (605) used in our previous study [50]. In addition, all L-CQDs show the "excitation wavelength dependence" of conventional L-CQDs. As the excitation wavelength increased, the emission wavelength of the L-CQDs exhibit a redshift. This is primarily due to the relaxation of polar groups (hydroxyl and carboxyl groups) on the surface of L-CQDs in polar solvents such as water and ethanol, resulting in a "giant red-edge effect" [51]. This may also be due to the uneven size of the L-CQDs, such that different particles have different responses to the excitation light with gradually increasing wavelength [52]. The QY of all L-CQDs are also significantly higher than that of the OL-CQDs.

The up-conversion (UP) performance of all L-CQDs was tested using near-infrared (NIR) light at 660–760 nm, and the results are shown in **Fig. S7a-d**. All L-CQDs also exhibited "excitation wavelength dependence" similar to the PL. The UP-PL intensity of L-CQDs-1 is the highest (963) among them, which is far greater than that of any of the CQDs prepared by hydrothermal treatment of lignin or doping with heteroatom groups [40, 50]. Interestingly, compared to our previous studies, the UP-PL intensity of L-CQDs is usually much weaker than the PL intensity. However, in this study, the UP-PL intensities of all the L-CQDs are still considerably high (Table 3), whereas OL-CQDs exhibited almost no UP-PL performance (**Fig. S8**). This may be due to the more abundant precursor composition that increased the surface defects of L-CQDs-1, which promoted the near-infrared absorption of L-CQDs, resulting in an increase in their UP-PL intensity. In summary, according to the PL and UP-PL fluorescence intensities of all the prepared L-CQDs, L-CQDs-1 prepared by the synergistic effect of the supercritical reaction and catalyst have higher utilization potential than other L-CQDs.

Table 3
Optical Properties of L-CQDs samples

Samples	Optimal EX (nm)	Optimal EM (nm)	PL intensity	Optimal UP-EX (nm)	Optimal UP-EM (nm)	UP intensity	QY (%)
OL-CQDs	470	531	63	750	504	16.3	1.07
L-CQDs-1	340	415	975	690	416	963	16.60
L-CQDs-2	320	428	986	680	437	599	16.78
L-CQDs-3	310	380	963	680	412	501	16.39
L-CQDs-4	320	386	1143	690	417	702	19.45

3.3 Chemical properties of L-CQDs

Figure 3 shows the chemical properties of the L-CQDs as measured by FTIR and XPS. As shown in Fig. 3a, the FTIR spectra of all L-CQDs are similar, indicating that they have the same functional group compositions, such as O–H at 3370 cm^{-1} [53, 54], C–H at 2930 cm^{-1} [55], C = O at 1720 cm^{-1} [56, 57], C = C at 1600 cm^{-1} [58], C–OH at 1400 cm^{-1} [56], C–O at 1120 cm^{-1} [59], aromatic C–H located near 1120 cm^{-1} [60], and C–O–C located near 1030 cm^{-1} [61].

The surface element compositions and functional group contents of all the L-CQDs were further characterized by XPS. As shown in Fig. 3b, the two strong peaks located at 284.8 and 533.5 eV belong to C 1s and O1 s, respectively, indicating that the all obtained L-CQDs have the same elemental composition and are primarily composed of C and O. However, there is little difference in the elemental contents of the four types of L-CQDs, among which the oxygen content of L-CQDs-1 is higher and the C/O ratio is lower, manifesting that their surface has more oxygen-containing defects, leading to a proper red shift of its wavelength and better PL and UP-PL performance (Table 3). This can be observed in Fig. 3c-f that the C 1*s* spectra of all obtained L-CQDs can be deconvoluted into three main peaks, which are C = C/C–C graphitic carbon near 284.4 eV, C-O near 285.8 eV, and C = O around 288.6 eV [62]. Among them, L-CQDs-4 have the highest graphitic carbon content and a higher degree of graphitization; therefore, their emission wavelength is still in the UV region compared with the other samples. However, L-CQDs-2 have the lowest degree of graphitization and more oxygen-containing defects on the surface in all L-CQDs; therefore, they have a larger optimal emission wavelength (428 nm) than the others (Table 3). As shown in Fig. 3g-j, the O 1s spectra of the four samples can be deconvoluted into two peaks at 531.9 and 592.9 eV, ascribed to C = O and C–OH [63], respectively. Among of all L-CQDs, L-CQDs-1 have the highest content of C–OH/C–O–C and demonstrate better fluorescence performance (Table 3) due to the presence of more abundant

electron-donating substituents on their surface, thus increasing the conjugated π structure density and enhancing the fluorescence intensity by forming p-π conjugation with the aromatic structure. Combining the results of C 1*s* and O 1*s*, the L-CQDs are comprised of various hydrophobic (carbon–carbon bonds) and hydrophilic groups (aldehyde-carbonyl and carboxyl-hydroxyl groups). The results of the XPS analysis are consistent with those of the FTIR.

3.4 Topological properties of L-CQDs

TEM and AFM were used to analyze the topological properties of the four types of L-CQDs, and the results are shown in Fig. 4. All L-CQDs particles are independent individuals with good dispersion by TEM and AFM, indicating that they have good water dispersibility, which may be related to the interaction between hydrophilic and hydrophobic groups on the surface of the L-CQDs [45, 64]. The inner images of Fig. 4a, c, e, g are high-resolution TEM images of the L-CQD samples. The results indicate that the surfaces of all L-CQD samples have uniform lattice fringes with a spacing of 0.21 nm, corresponding to the (001) crystal plane of carbon [65]. This further indicates that the four types of L-CQDs had a high degree of graphitization. The diameters of 100 individual particles of each L-CQD sample were randomly measured using Nano Measurer 1.2 software, and their particle size distributions were obtained, as shown in Fig. 4b, d, f, h. The particle size distributions of these L-CQDs range from 1.0 to 6.0 nm and the average particle sizes of L-CQDs-1, L-CQDs-2, L-CQDs-3, and L-CQDs-4 are 4.01, 2.81, 3.17, and 3.06 nm, respectively. The sizes of the obtained L-CQDs conform to the traditional CQDs size standard (less than 10 nm). Among them, L-CQDs-1 have the largest average particle size, which is primarily related to the more abundant compound composition of the precursor CL-1. This provided more available small molecules for the formation of L-CQDs-1 in the reaction, improving their polymerization efficiency and increasing their size under the same reaction time. According to the quantum confinement effect [66, 67], combined with the optical properties of L-CQDs (Fig. 2), the increase in the particle size of L-CQDs-1 lead to a significant red shift in the wavelength to the visible light range and improve its relative fluorescence intensity laterally. As observed from the AFM images of the four L-CQD samples in Fig. 4i-p, they exhibit good dispersion and their maximum height is between 2.6–6.3 nm, which is consistent with the TEM analysis results.

3.5 Speculation on the formation mechanism of L-CQDs

Under supercritical reaction conditions, the solvent ethanol removes two hydrogen atoms in lignin and generates H_2 on Pd/C catalyst, as shown in formula 3. Then, under high temperature and pressure, the H_2 breaks the ether or carbon–carbon bonds connecting the structural units of lignin and binds to the broken end to form a phenolic hydroxyl group, leading to the cracking of lignin into small molecules. According to the XPS and TEM results, the L-CQDs have a highly graphitized structure, which is related to the presence of a large number of aromatic compounds in the precursor CL. Compared with the original alkali lignin with a large molecular weight, CL containing more aromatic monomers can facilitate unidirectional polymerization between them. The reduction in the lignin molecular weight also makes the heat distribution of the reaction more uniform, avoiding the local carbonization of lignin. In the early stages of the reaction, several cracked lignin monomers are repolymerized and dehydrated to form a relatively

stable structure [68]. Then, other small molecules such as degraded linear or branched small molecules or incompletely cleaved dimers, trimers, or larger molecules participate in the repolymerization, increasing the size of the L-CQDs. For example, among of all L-CQDs, L-CQDs-1 can emit bright blue light under 365 nm UV and NIR light (Fig. 2b). This is mainly because the much abundant compound compositions in CL-1 precursor increase the surface defects of L-CQDs-1, which in turn enhance their radiative transition to UV and NIR light. Simultaneously, the suitable size of L-CQDs-1 enables their emission wavelength to be in the visible-light range, preventing it from being too intense but invisible. Inversely, in the hydrothermal process of the original alkali lignin, only a small amount of H^+ ionized by H_2O breaks the lignin bonds, and most of the bonds are carbonized without a reaction, resulting in a limited number of small molecules to participate in the polymerization reaction of OL-CQD. The reaction system has no direction and is chaotic; therefore, the fluorescence performance of the OL-CQDs is poor. In conclusion, the reaction pathway of lignin-forming L-CQDs was regulated to a great extent and improved using a two-step method, and high-performance L-CQDs were successfully prepared without doping reagents. The formation mechanism of the L-CQDs is shown in Scheme 2.

$$2\,CH_3CH_2OH \xrightarrow{260℃,Pd/C} 2\,CH_3CHO + H_2\uparrow \quad (3)$$

3.6 Biological imaging and targeted recognition of tumor cells

Before cell imaging, the cytotoxicity of L-CQDs-1, OL-CQDs, and FA@L-CQDs-1 on human HepG2 and L02 cells was tested, and the results are shown in **Fig. S9a, b**. At a concentration of 1 mg/mL, the survival rates of the two types of cells cultured with the three samples are all above 90%, which indicates that they have low toxicity. The cell-imaging capabilities of L-CQDs-1 and OL-CQDs were tested using the above two types of cells. The excitation wavelengths of the laser confocal microscope were fixed at 405 and 635 nm, which were used to simulate UV-vis and NIR light, respectively. The results are shown in Fig. 5. Compared to the bright and merged fields, L-CQDs-1 successfully entered the interior of HepG2 and L02 cells. Because L-CQDs-1 have both high PL intensity and UP-PL intensity, regardless of whether the excitation light was 405 nm or 635 nm, obvious cell contours in HepG2 and L02 cells were seen. However, when the OL-CQDs were used to cultivate cells, the fluorescence signal is difficult to detect in the image because of their weak fluorescence intensity. Thus, the L-CQDs-1 prepared in this study significantly improved their ability for cell imaging compared with the traditional OL-CQDs prepared by a simple one-pot hydrothermal method.

FA was combined with L-CQDs-1 via a fluorescence quenching coupling reaction to obtain the FA@L-CQDs-1 quenched fluorescence probe. As shown in Fig. 6a, the fluorescence intensity of FA@L-CQDs-1 is only approximately a quarter of that of the L-CQDs. Since most cancer cells have a large number of folate receptors on their surfaces, when the quenched FA@L-CQDs-1 enters the cell, FA binds to the folate receptor and falls off the surface of L-CQDs-1, and L-CQDs-1 can re-emit fluorescence [69] (Fig. 6b). However, normal cells have very low levels of folate receptors on their surfaces; therefore, FA@L-CQDs-1

remains in a quenched state in normal cells, and the fluorescence emitted by the cells is weak. As shown in Fig. 6c, FA@L-CQDs-1 can emit bright blue fluorescence in HepG2 cells under the irradiation of 405 nm and 635 nm lasers; however, the intensity is weaker than that of cells cultured with L-CQDs-1 alone (Fig. 5). This may be because FA on the surface of L-CQDs-1 is not fully bound by folate receptors, leading to a decrease in the number of exfoliated CQDs. However, in L02 cells, the fluorescence signal was much weaker than that of in HepG2 cells, and cell morphology hardly is identified. In this study, we successfully prepared FA@L-CQDs-1 to achieve the targeted differentiation of HepG2 cancer cells from normal cells.

After the experiment, FA@L-CQDs-1 were injected into the tail vein of a tumor-bearing nude mouse to test the labelling ability of FA@L-CQDs-1. The results are shown in Fig. 7. Thirty min after injection, the fluorescence signal gradually appeared in the mice, and the tumor also indicated weak fluorescence (Fig. 7a, 30 **min**). When the injection time was extended to 2–4 h, the fluorescence signal area in mice further spread to the whole body, and the fluorescence signal in the tumor was significantly stronger than that of in other locations (Fig. 7a, 2 & 4h). This is due to the strong fluorescence being re-emitted by L-CQDs-1 after the folate receptor in FA@L-CQDs-1 binds to the tumor. 12 h after injection, compared to 4 h, the area and intensity of the fluorescence signal in the mouse gradually weakened; however, the tumor site still maintained a high fluorescence intensity, indicating that FA@L-CQDs-1 can be normally metabolized in mouse tissues (Fig. 7a, 12h). Furthermore, 24 h after injection, the fluorescence signals of other organs in the mouse essentially disappeared, and a high fluorescence intensity remained only at the tumor site (Fig. 7a, 24h). Above results manifest that FA@L-CQDs-1 can specifically mark the tumor site by comparing the fluorescence intensity and exists in the tumor site longer than in other tissues. The nude mice were euthanized 24 h after the injection, and the major organs were removed. As shown in Fig. 7b, strong fluorescence signals were observed in the lungs, liver, kidneys, and tumor sites of the mice. Among them, the kidney and tumor sites have the strongest fluorescence intensity, which indicates that FA@L-CQDs-1 is primarily metabolized by the kidneys and assisted by the liver and respiratory system. Moreover, FA@L-CQDs-1 can stably accumulate at tumor sites and can thus be used as a safe tumor labelling reagent. In addition, another mouse injected with the FA@L-CQDs-1 solution survived for a week. Combined with the low cytotoxicity of FA@L-CQDs-1, it can be considered that FA@L-CQDs-1 has good biocompatibility and is a safe tumor labelling reagent.

4 Conclusion

A two-step strategy was developed to efficiently prepare lignin-based CQDs with high fluorescence properties. Lignin was first cracked using an ethanol supercritical/noble metal catalyst, and then the L-CQDs were prepared with the cracked lignin products without adding any heteroatom reagents. CL-1 prepared by the catalytic activity of Pt/C under supercritical conditions contains more abundant compounds and the lowest relative molecular weight among the prepared CL samples, which is an excellent precursor to prepare L-CQDs-1. Compared with the OL-CQDs prepared by the traditional one-pot hydrothermal method, the fluorescence intensity and up-conversion photoluminescence of L-CQDs-1 were increased from 63 to 975, and from 16.3 to 963, which significantly enhanced by about 15 times and 60 times, respectively. L-CQDs-1 emit bright blue light under 365-nm UV and NIR light. Additionally, using FA

to quench L-CQDs-1, the prepared FA@L-CQDs-1 can target and label tumor cells through cell-inside fluorescence recovery. This study is highly significant for improving the fluorescence intensity of biomass-based CQDs and broadening their applications.

Declarations

Supplementary information

The online version contains supplementary material available at

Funding The project was sponsored by the National Key Research and Development Program of China (Grant No. 2021YFE0114400), National Natural Science Foundation of China (Grant No. 22268007), Natural Science Foundation of Guangxi Province, China (Grant No. 2021GXNSFDA196006), and the Foundation of Guangxi Key Laboratory of Clean Pulp & Papermaking and Pollution Control, College of Light Industry and Food Engineering, Guangxi University (Grant Nos. 2021KF20, 2021KF02, 2021KF32, and 2021KF34). The AJR efforts were provided by the University of Tennessee.

Conflict of interest The authors declare no competing interests.

Authorship contribution statement

Xueping Song supervised the project. Siyu Zhao and Guihua Yue designed the experiments. Xiaoli Liu, Shiru Qin and Baosu Wang performed the experiments. All authors discussed experiments and results. Siyu Zhao wrote the manuscript. Peitao Zhao, Arthur J. Ragauskas and Min Wu revised the manuscript. All authors have given approval to the final version of the manuscript.

References

1. Xu X, Ray R, Gu Y, Ploehn HJ, Gearheart LA, Raker K, Scrivens WA (2004) Electrophoretic analysis and purification of fluorescent single-walled carbon nanotube fragments. J Am Chem Soc 126 (40):12736-12737. https://doi.org/10.1021/ja040082h
2. Gonçalves H, Jorge PAS, Fernandes JRA, Esteves da Silva JCG (2010) Hg(II) sensing based on functionalized carbon dots obtained by direct laser ablation. Sens Actuator B-Chem 145 (2):702-707. https://doi.org/10.1016/j.snb.2010.01.031
3. Tao H, Yang K, Ma Z, Wan J, Zhang Y, Kang Z, Liu Z (2012) In vivo NIR fluorescence imaging, biodistribution, and toxicology of photoluminescent carbon dots produced from carbon nanotubes and graphite. Small 8 (2):281-290. https://doi.org/10.1002/smll.201101706
4. LeCroy GE, Sonkar SK, Yang F, Veca LM, Wang P, Tackett KN, Yu JJ, Vasile E, Qian HJ, Liu YM, Luo P, Sun YP (2014) Toward Structurally Defined Carbon Dots as Ultracompact Fluorescent Probes. ACS Nano 8 (5):4522-4529. https://doi.org/10.1021/nn406628s

5. Hu S, Chang Q, Lin K, Yang J (2016) Tailoring surface charge distribution of carbon dots through heteroatoms for enhanced visible-light photocatalytic activity. Carbon 105:484-489. https://doi.org/10.1016/j.carbon.2016.04.078
6. Hu S, Yang W, Li N, Wang H, Yang J, Chang Q (2018) Carbon-Dot-Based Heterojunction for Engineering Band-Edge Position and Photocatalytic Performance. Small 14 (44):e1803447. https://doi.org/10.1002/smll.201803447
7. Achilleos DS, Yang W, Kasap H, Savateev A, Markushyna Y, Durrant JR, Reisner E (2020) Solar Reforming of Biomass with Homogeneous Carbon Dots. Angew Chem Int Ed 59 (41):18184-18188. https://doi.org/10.1002/anie.202008217
8. Tao X, Liao M, Wu F, Jiang Y, Sun J, Shi S (2022) Designing of biomass-derived carbon quantum dots@polyvinyl alcohol film with excellent fluorescent performance and pH-responsiveness for intelligent detection. Chem Eng J 443:136442. https://doi.org/10.1016/j.cej.2022.136442
9. Zhou P, Xu J, Hou X, Dai L, Xiao X, Zhang C, Huo K (2022) Lignin fractionation-inspired carbon dots to enable trimodule fluorescent sensing of pH, silver ion and cysteine. Ind Crop Prod 185:115127. https://doi.org/10.1016/j.indcrop.2022.115127
10. Bai Y, Zhao J, Zhang L, Wang S, Hua J, Zhao S, Liang H (2022) A Smart Near-Infrared Carbon Dot-Metal Organic Framework Assemblies for Tumor Microenvironment-Activated Cancer Imaging and Chemodynamic-Photothermal Combined Therapy. Adv Healthc Mater 11 (12):e2102759. https://doi.org/10.1002/adhm.202102759
11. Gu M, Lee D-Y, Mun J, Kim D, Cho H-i, Kim B, Kim W, Lee G, Kim B-S, Kim H-i (2022) Solar-to-hydrogen peroxide conversion of photocatalytic carbon dots with anthraquinone: Unveiling the dual role of surface functionalities. Appl Catal B-Environ 312:121379. https://doi.org/10.1016/j.apcatb.2022.121379
12. Liu Y, Zhou P, Wu Y, Su X, Liu H, Zhu G, Zhou Q (2022) Fast and efficient "on-off-on" fluorescent sensor from N-doped carbon dots for detection of mercury and iodine ions in environmental water. Sci Total Environ 827:154357. https://doi.org/10.1016/j.scitotenv.2022.154357
13. Mauro N, Utzeri MA, Sciortino A, Messina F, Cannas M, Popescu R, Gerthsen D, Buscarino G, Cavallaro G, Giammona G (2022) Decagram-Scale Synthesis of Multicolor Carbon Nanodots: Self-Tracking Nanoheaters with Inherent and Selective Anticancer Properties. ACS Appl Mater Interfaces 14 (2):2551-2563. https://doi.org/10.1021/acsami.1c19599
14. Jo M-H, Kim K-H, Ahn H-J (2022) P-doped carbon quantum dot graft-functionalized amorphous WO3 for stable and flexible electrochromic energy-storage devices. Chem Eng J 445:136826. https://doi.org/10.1016/j.cej.2022.136826
15. Guo J, Xu J, Liu X, Dai L, Zhang C, Xiao X, Huo K (2022) Enabling dual valorization of lignocellulose by fluorescent lignin carbon dots and biochar-supported persulfate activation: Towards waste-treats-pollutant. J Hazard Mater 435:129072. https://doi.org/10.1016/j.jhazmat.2022.129072
16. Song X, Zhao S, Xu Y, Chen X, Wang S, Zhao P, Pu Y, Ragauskas AJ (2022) Preparation, Properties, and Application of Lignocellulosic-Based Fluorescent Carbon Dots. ChemSusChem:e202102486.

https://doi.org/10.1002/cssc.202102486

17. Zhu L, Shen D, Wang Q, Luo KH (2021) Green Synthesis of Tunable Fluorescent Carbon Quantum Dots from Lignin and Their Application in Anti-Counterfeit Printing. ACS Appl Mater Interfaces 13 (47):56465-56475. https://doi.org/10.1021/acsami.1c16679
18. Gan J, Wu Y, Yang F, Zhang H, Wu X, Wang Y, Xu R (2022) Wood-cellulose photoluminescence material based on carbon quantum dot for light conversion. Carbohydr Polym 290:119429. https://doi.org/10.1016/j.carbpol.2022.119429
19. Zhao X, Zhang L, Liu D (2012) Biomass recalcitrance. Part I: the chemical compositions and physical structures affecting the enzymatic hydrolysis of lignocellulose. Biofuels Bioprod Biorefining 6 (4):465-482. https://doi.org/10.1002/bbb.1331
20. Liu, W., Liu, K., Wang, Y., Lin, Q., Liu, J., Du, H., et al. (2022) Sustainable production of cellulose nanofibrils from Kraft pulp for the stabilization of oil-in-water Pickering emulsions. Ind Crop Prod 185: 115123. https://doi.org/10.1016/j.indcrop.2022.115123
21. Liu, K., Du, H., Zheng, T., Liu, W., Zhang, M., Liu, H., et al. (2021) Lignin-containing cellulose nanomaterials: preparation and applications. Green Chem 23(24): 9723–9746. https://doi.org/10.1039/D1GC02841C
22. Liu, W., Liu, K., Du, H., Zheng, T., Zhang, N., Xu, T., et al. (2022) Cellulose Nanopaper: Fabrication, Functionalization, and Applications. Nano-Micro Lett 14(1): 104. https://doi.org/10.1007/s40820-022-00849-x
23. Liu, H., Du, H., Zheng, T., Liu, K., Ji, X., Xu, T., Zhang, X., et al. (2021) Cellulose based composite foams and aerogels for advanced energy storage devices. Chem Eng J 426: 130817. https://doi.org/10.1016/j.cej.2021.130817
24. Zhang, M., Du, H., Liu, K., Nie, S., Xu, T., Zhang, X., & Si, C. (2021) Fabrication and applications of cellulose-based nanogenerators. Adv Compos Hybrid Mater 4: 865–884. https://doi.org/10.1007/s42114-021-00312-2
25. Liu, S., Du, H., Liu, K., Ma, M.-G., Kwon, Y.-E., Si, C., Ji, X.-X., et al. (2021) Flexible and porous Co_3O_4-carbon nanofibers as binder-free electrodes for supercapacitors. Adv Compos Hybrid Mater 4(4): 1367–1383. https://doi.org/10.1007/s42114-021-00344-8
26. Xiao L., Qi H., Qu K., Shi C., Cheng Ya., Sun Z., Yuan B., et al.(2021) Layer-by-layer assembled free-standing and flexible nanocellulose/porous Co_3O_4 polyhedron hybrid film as supercapacitor electrodes. Adv Compos Hybrid Mater 4: 306-316. https://doi.org/10.1007/s42114-021-00223-2
27. Xu, T., Du, H., Liu, H., Liu, W., Zhang, X., Si, C., et al. (2021) Advanced Nanocellulose-Based Composites for Flexible Functional Energy Storage Devices. Adv Mater 33(48): 2101368. https://doi.org/10.1002/adma.202101368
28. Xu, T., Liu, K., Sheng, N., Zhang, M., Liu, W., Liu, H., et al. (2022) Biopolymer-based hydrogel electrolytes for advanced energy storage/conversion devices: Properties, applications, and perspectives. Energy Storage Mater 48: 244–262. https://doi.org/10.1016/j.ensm.2022.03.013

29. Qu K., Sun Z., Shi C., Wang W., Xiao L., Tian J., Huang Z., Guo Z. (2021) Correction to: Dual-acting cellulose nanocomposites filled with carbon nanotubes and zeolitic imidazolate framework-67 (ZIF-67)–derived polyhedral porous Co_3O_4 for symmetric supercapacitors. Adv Compos Hybrid Mater 4:670-683. https://doi.org/10.1007/s42114-021-00328-8
30. Liu, K., Du, H., Liu, W., Zhang, M., Wang, Y., Liu, H., et al. (2022) Strong, flexible, and highly conductive cellulose nanofibril/PEDOT:PSS/MXene nanocomposite films for efficient electromagnetic interference shielding. Nanoscale 14: 14902-14912. https://doi.org/10.1039/D2NR00468B
31. Du B., Zhang D., Qian J., Cai M., He C., Zhou P. & Shui A. (2021) Multifunctional carbon nanofiber-SiC nanowire aerogel films with superior microwave absorbing performance. Adv Compos Hybrid Mater 4:1281–1291. https://doi.org/10.1007/s42114-021-00286-1
32. Liu, K., Du, H., Liu, W., Liu, H., Zhang, M., Xu, T., & Si, C. (2022) Cellulose Nanomaterials for Oil Exploration Applications. Polym Rev 62(3): 585–625. https://doi.org/10.1080/15583724.2021.2007121
33. Liu, H., Xu, T., Cai, C., Liu, K., Liu, W., Zhang, M., et al. (2022) Multifunctional Superelastic, Superhydrophilic, and Ultralight Nanocellulose-Based Composite Carbon Aerogels for Compressive Supercapacitor and Strain Sensor. Adv Funct Mater 32(26): 2113082. https://doi.org/10.1002/adfm.202113082
34. Zhu E. Xu G., Ye X., Yang J., Yang H., Wang D., Shi Z., Deng J. (2021) Preparation and characterization of hydrothermally pretreated bamboo powder with improved thermoplasticity by propargyl bromide modification in a heterogeneous system. Adv Compos Hybrid Mater 4: 1059-1069. https://doi.org/10.1007/s42114-021-00316-y
35. Gu H., Gao C., Zhou X., Du A., Naik N., Guo Z., (2021). Nanocellulose nanocomposite aerogel towards efficient oil and organic solvent adsorption. Adv Compos Hybrid Mater 4: 459-468. https://doi.org/10.1007/s42114-021-00289-y
36. Ou L, Dou C, Yu JH, Kim H, Park YC, Park S, Kelley S, Lee EY (2020) Techno-economic analysis of sugar production from lignocellulosic biomass with utilization of hemicellulose and lignin for high-value co-products. Biofuels Bioprod Biorefining 15 (2):404-415. https://doi.org/10.1002/bbb.2170
37. Ma M, Dai L, Si C, Hui L, Liu Z, Ni Y (2019) A Facile Preparation of Super Long-Term Stable Lignin Nanoparticles from Black Liquor. ChemSusChem 12 (24):5239-5245. https://doi.org/10.1002/cssc.201902287
38. Jiang ZY, Zhang XH, Sun W, Yang DR, Duchesne PN, Gao YG, Wang ZY, Yan TJ, Yuan ZM, Yang GH, Ji XX, Chen JC, Huang BB, Ozin GA (2019) Building a Bridge from Papermaking to Solar Fuels. Angew Chem Int Ed 58 (42):14850 –14854. https://doi.org/10.1002/ange.201909222
39. Wu Q, Yu S, Hao N, Wells T, Meng X, Li M, Pu Y, Liu S, Ragauskas AJ (2017) Characterization of products from hydrothermal carbonization of pine. Bioresour Technol 244:78-83. https://doi.org/10.1016/j.biortech.2017.07.138
40. Zhao S, Song X, Chai X, Zhao P, He H, Liu Z (2020) Green production of fluorescent carbon quantum dots based on pine wood and its application in the detection of Fe3+. J Clean Prod 263:121561.

https://doi.org/10.1016/j.jclepro.2020.121561

41. Chen W, Hu C, Yang Y, Cui J, Liu Y (2016) Rapid synthesis of carbon dots by hydrothermal treatment of lignin. Materials 9 (3):184. https://doi.org/10.3390/ma9030184
42. Xu X, Sun Q, Ma Y, Jiang X, Niu N, Chen L (2022) Synthesis of KCl-doped lignin carbon dots nanoenzymes for colorimetric sensing glutathione in human serum. Sens Actuator B-Chem 364:131881. https://doi.org/10.1016/j.snb.2022.131881
43. Zhuang J, Ren S, Zhu B, Han C, Li Y, Zhang X, Gao H, Fan M, Tian Q (2022) Lignin-based carbon dots as high-performance support of Pt single atoms for photocatalytic H2 evolution. Chem Eng J 446:136873. https://doi.org/10.1016/j.cej.2022.136873
44. Zhu L, Shen D, Hong Luo K (2022) Triple-emission nitrogen and boron co-doped carbon quantum dots from lignin: Highly fluorescent sensing platform for detection of hexavalent chromium ions. J Colloid Interface Sci 617:557-567. https://doi.org/10.1016/j.jcis.2022.03.039
45. Zhao S, Chen X, Zhang C, Zhao P, Ragauskas AJ, Song X (2021) Fluorescence enhancement of lignin-based carbon quantum dots by concentration-dependent and electron-donating substituent synergy and their cell imaging applications. ACS Appl Mater Interfaces 13 (51): 61565-61577. https://doi.org/10.1021/acsami.1c20648
46. Church JM, Joshi HK (1951) Acetaldehyde by Dehydrogenation of Ethyl Alcohol. Ind Eng Chem 43 (8):1804–1811. https://doi.org/10.1021/ie50500a035
47. Tran MH, Phan DP, Nguyen TH, Kim HB, Kim J, Park ED, Lee EY (2021) Catalytic hydrogenolysis of alkali lignin in supercritical ethanol over copper monometallic catalyst supported on a chromium-based metal-organic framework for the efficient production of aromatic monomers. Bioresour Technol 342:125941. https://doi.org/10.1016/j.biortech.2021.125941
48. Biswas B, Kumar A, Kaur R, Krishna BB, Bhaskar T (2021) Catalytic hydrothermal liquefaction of alkali lignin over activated bio-char supported bimetallic catalyst. Bioresour Technol 337:125439. https://doi.org/10.1016/j.biortech.2021.125439
49. Jeong Y, Moon K, Jeong S, Koh W, Lee K (2018) Converting waste papers to fluorescent carbon dots in the recycling process without loss of ionic liquids and bioimaging applications. ACS Sustain Chem Eng 6 (4):4510-4515. https://doi.org/10.1021/acssuschemeng.8b00353
50. Zhao S, Chen X, Zhang C, Zhao P, Ragauskas AJ, Song X (2021) Fluorescence enhancement of lignin-based carbon quantum dots by concentration-dependent and electron-donating substituent synergy and their cell imaging applications. ACS Appl Mater Interfaces 13 (51): 61565–61577. https://doi.org/10.1021/acsami.1c20648
51. Cushing SK, Li M, Huang F, Wu N (2014) Origin of strong excitation wavelength dependent fluorescence of graphene oxide. ACS Nano 8 (1):1002-1013. https://doi.org/10.1021/nn405843d
52. Wen Z-H, Yin X-B (2016) Excitation-independent carbon dots, from photoluminescence mechanism to single-color application. RSC Adv 6 (33):27829-27835. https://doi.org/10.1039/c5ra27172j
53. Souza DRdS, Mesquita JPd, Lago RM, Caminhas LD, Pereira FV (2016) Cellulose Nanocrystals: A Versatile Precursor for the Preparation of Different Carbon Structures and Luminescent Carbon Dots.

Ind Crop Prod 93:121-128. https://doi.org/10.1016/j.indcrop.2016.04.073

54. Liu H, Xu T, Liang Q, Zhao Q, Zhao D, Si C (2022) Compressible cellulose nanofibrils/reduced graphene oxide composite carbon aerogel for solid-state supercapacitor. Adv Compos Hybrid Mater 5:1168-1179. https://doi.org/10.1007/s42114-022-00427-0
55. Yang Q, Duan J, Yang W, Li X, Mo J, Yang P, Tang Q (2018) Nitrogen-doped Carbon Quantum Dots from Biomass Via Simple One-pot Method and Exploration of Their Application. Appl Surf Sci 434:1079-1085. https://doi.org/10.1016/j.apsusc.2017.11.040
56. Liu Z, Chen M, Guo Y, Zhou J, Shi Q, Sun R (2020) Oxidized Nanocellulose Facilitates Preparing Photoluminescent Nitrogen-doped Fluorescent Carbon Dots for Fe^{3+} Ions Detection and Bioimaging. Chem Eng J 384:123260. https://doi.org/10.1016/j.cej.2019.123260
57. Liu K, Liu W, Li W, Duan Y, Zhou K, Zhang S, Ni S, Xu T, Du H, Si C (2022) Strong and highly conductive cellulose nanofibril/silver nanowires nanopaper for high performance electromagnetic interference shielding. Adv Compos Hybrid Mater 5:1078-1089. https://doi.org/10.1007/s42114-022-00425-2
58. Jiang X, Huang J, Chen T, Zhao Q, Xu F, Zhang X (2020) Synthesis of Hemicellulose/deep Eutectic Solvent Based Carbon Quantum Dots for Ultrasensitive Detection of Ag(+) and L-cysteine with "off-on" Pattern. International journal of biological macromolecules 153:412-420. https://doi.org/10.1016/j.ijbiomac.2020.03.026
59. Atchudan R, Edison T, Lee YR (2016) Nitrogen-doped Carbon Dots Originating from Unripe Peach for Fluorescent Bioimaging and Electrocatalytic Oxygen Reduction Reaction. J Colloid Interface Sci 482:8-18. https://doi.org/10.1016/j.jcis.2016.07.058
60. Ding Z, Li F, Wen J, Wang X, Sun R (2018) Gram-scale Synthesis of Single-crystalline Graphene Quantum Dots Derived from Lignin Biomass. Green Chem 20 (6):1383-1390. https://doi.org/10.1039/c7gc03218h
61. Liu M, Xu Y, Niu F, Gooding JJ, Liu J (2016) Carbon Quantum Dots Directly Generated from Electrochemical Oxidation of Graphite Electrodes in Alkaline Alcohols and The Applications for Specific Ferric Ion Detection and Cell Imaging. Analyst 141 (9):2657-2664. https://doi.org/10.1039/c5an02231b
62. Li Y, Tang Z, Pan Z, Wang R, Wang X, Zhao P, Liu M, Zhu Y, Liu C, Wang W, Liang Q, Gao J, Yu Y, Li Z, Lei B, Sun J (2022) Calcium-Mobilizing Properties of Salvia miltiorrhiza-Derived Carbon Dots Confer Enhanced Environmental Adaptability in Plants. ACS Nano 16 (3):4357-4370. https://doi.org/10.1021/acsnano.1c10556
63. Zhang M, Zhang W, Fan X, Ma Y, Huang H, Wang X, Liu Y, Lin H, Li Y, Tian H, Shao M, Kang Z (2022) Chiral Carbon Dots Derived from Serine with Well-Defined Structure and Enantioselective Catalytic Activity. Nano Lett 22 (17):7203-7211. https://doi.org/10.1021/acs.nanolett.2c02674
64. Zhu Z, Yang P, Chen M, Zhang T, Cao Y, Zhang W, Zhou X, Chen W (2019) Microwave Synthesis of Amphiphilic Carbon Dots from Xylose and Construction of Luminescent Composites with Shape Recovery Performance. J Lumines 213:474-481. https://doi.org/10.1016/j.jlumin.2019.05.006

65. Xu Y, Wang B, Zhang M, Zhang J, Li Y, Jia P, Zhang H, Duan L, Li Y, Li Y, Qu X, Wang S, Liu D, Zhou W, Zhao H, Zhang H, Chen L, An X, Lu S, Zhang S (2022) Carbon Dots as a Potential Therapeutic Agent for the Treatment of Cancer-Related Anemia. Adv Mater 34 (19):e2200905. https://doi.org/10.1002/adma.202200905
66. Kim S, Hwang SW, Kim MK, Shin DY, Shin DH, Kim CO, Yang SB, Park JH, Hwang E, Choi SH (2012) Anomalous behaviors of visible luminescence from graphene quantum dots: interplay between size and shape. ACS Nano 6 (9):8203-8208. https://doi.org/10.1021/nn302878r
67. Zhu S, Song Y, Zhao X, Shao J, Zhang J, Yang B (2015) The photoluminescence mechanism in carbon dots (graphene quantum dots, carbon nanodots, and polymer dots): current state and future perspective. Nano Res 8 (2):355-381. https://doi.org/10.1007/s12274-014-0644-3
68. Yuan F, Yuan T, Sui L, Wang Z, Xi Z, Li Y, Li X, Fan L, Tan Z, Chen A, Jin M, Yang S (2018) Engineering triangular carbon quantum dots with unprecedented narrow bandwidth emission for multicolored LEDs. Nature communications 9 (1):2249. https://doi.org/10.1038/s41467-018-04635-5
69. Lai IP-J, Harroun SG, Chen S-Y, Unnikrishnan B, Li Y-J, Huang C-C (2016) Solid-state synthesis of self-functional carbon quantum dots for detection of bacteria and tumor cells. Sens Actuator B-Chem 228:465-470. https://doi.org/10.1016/j.snb.2016.01.062

Schemes

Schemes 1 and 2 are available in the Supplementary Files section.

Figures

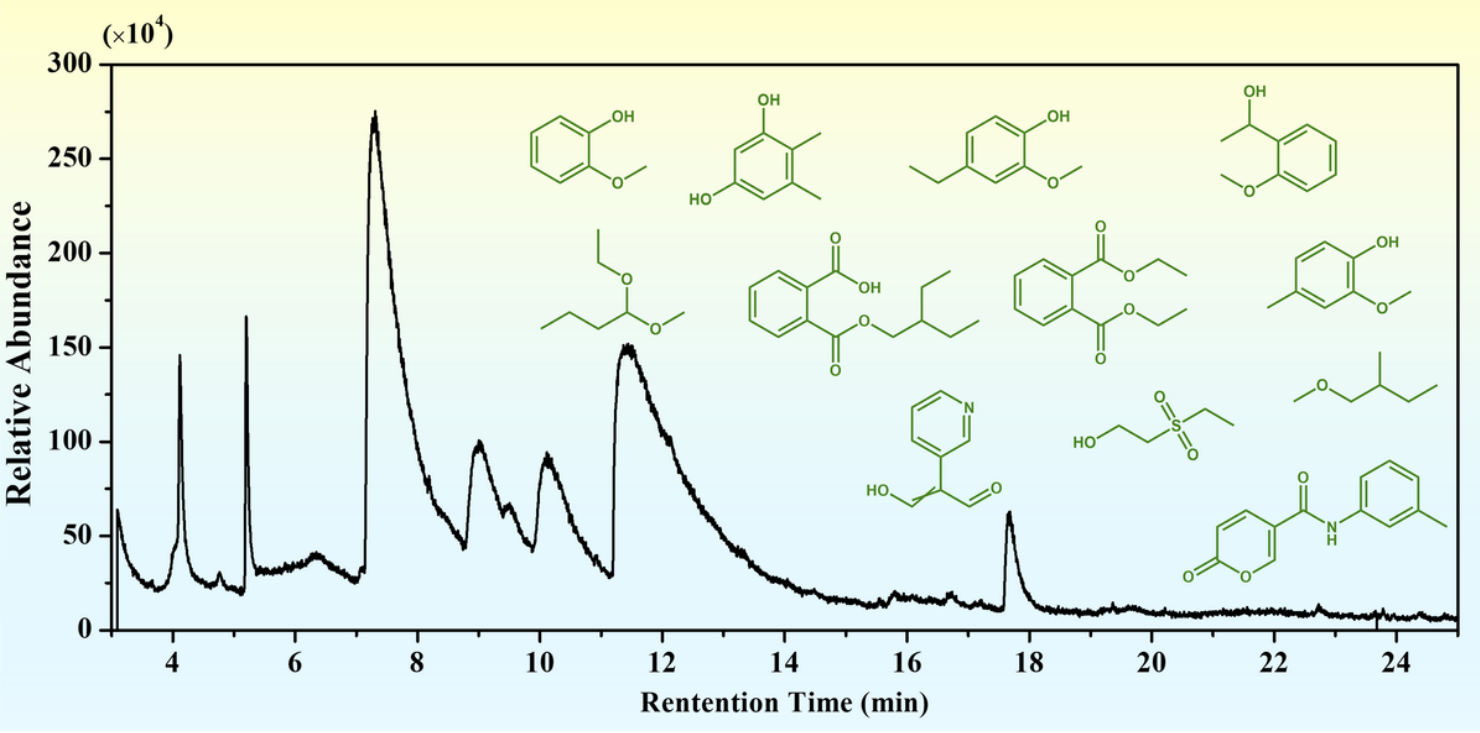

Figure 1

TIC spectra of CL-1 and its main low-molecular-weight compounds

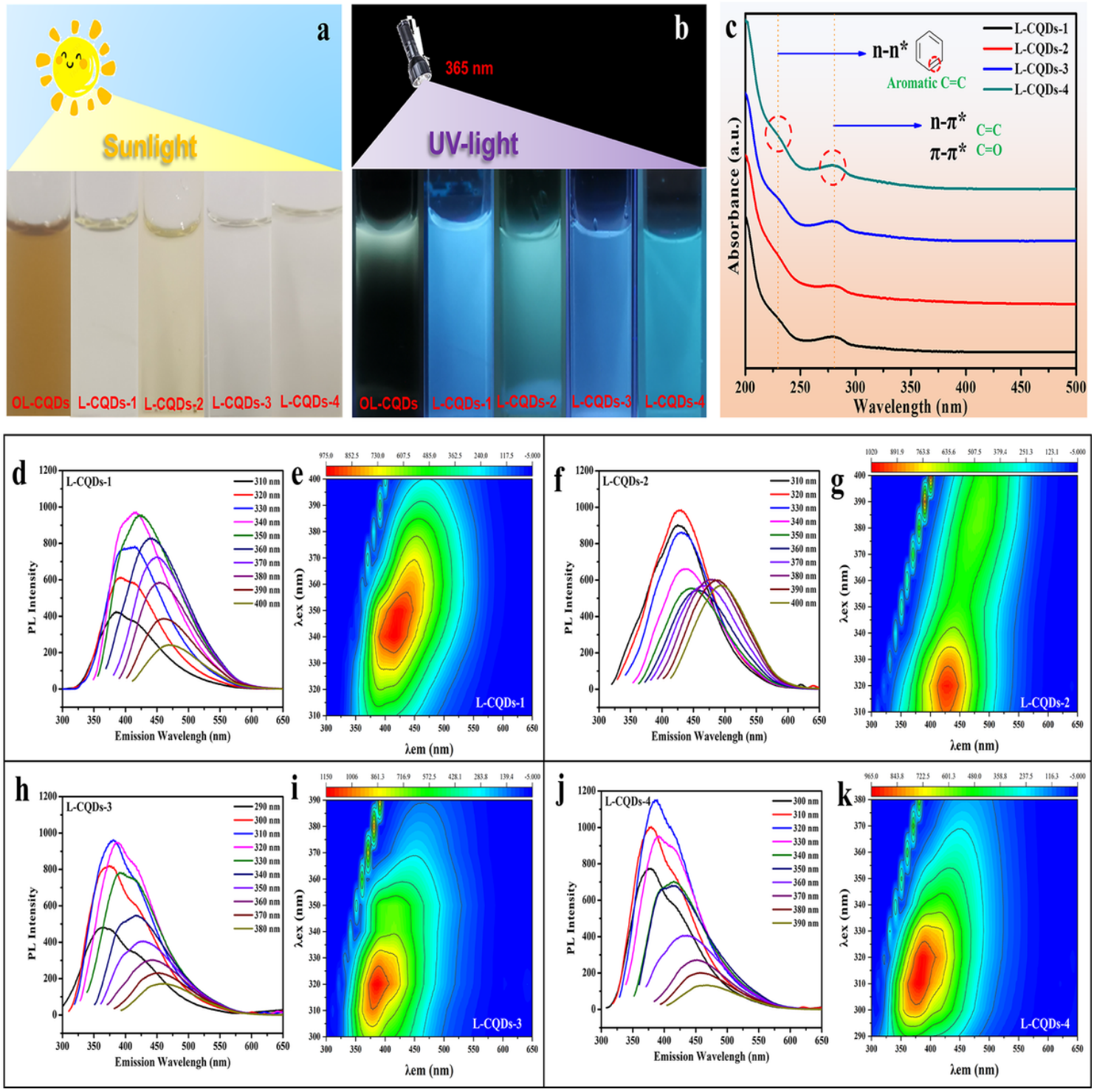

Figure 2

Photographs of L-CQDs under (**a**) sunlight and (**b**) 365 nm UV-light, and (**c**) UV-vis spectra. PL spectra of (**d**) L-CQDs-1, (**f**) L-CQDs-2, (**h**) L-CQDs-3, and (**j**) L-CQDs-4, and three-dimensional fluorescence spectra of (**e**) L-CQDs-1, (**g**) L-CQDs-2, (**i**) L-CQDs-3, and (**k**) L-CQDs-4.

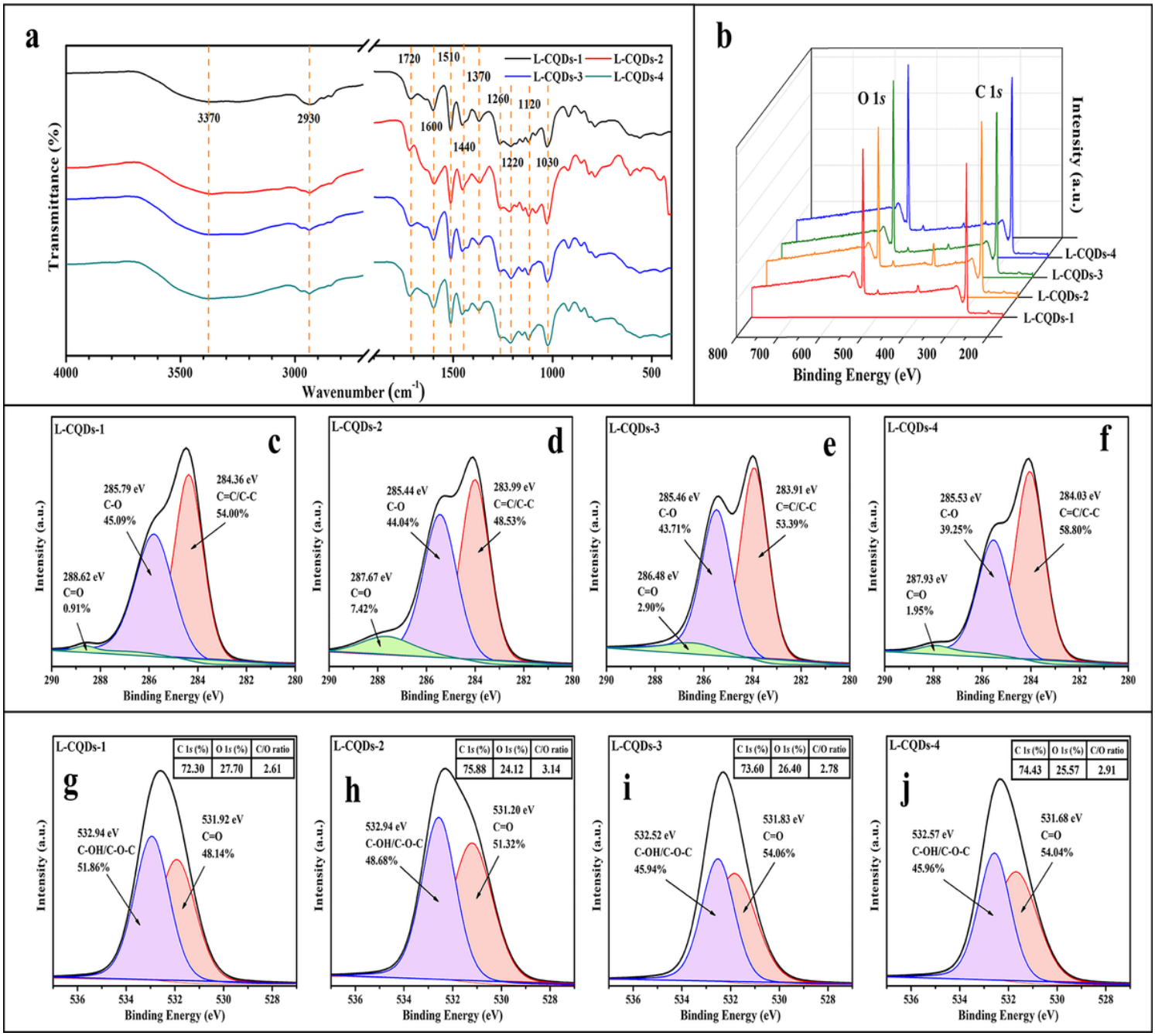

Figure 3

(**a**) FTIR spectra, (**b**) XPS full-spectrum scan of L-CQDs. C 1*s* high-resolution XPS fitting spectra generated for (**c**) L-CQDs-1, (**d**) L-CQDs-2, (**e**) L-CQDs-3, and (**f**) L-CQDs-4. O 1*s* high-resolution XPS fitting spectra generated for (**g**) L-CQDs-1, (**h**) L-CQDs-2, (**i**) L-CQDs-3, and (**j**) L-CQDs-4.

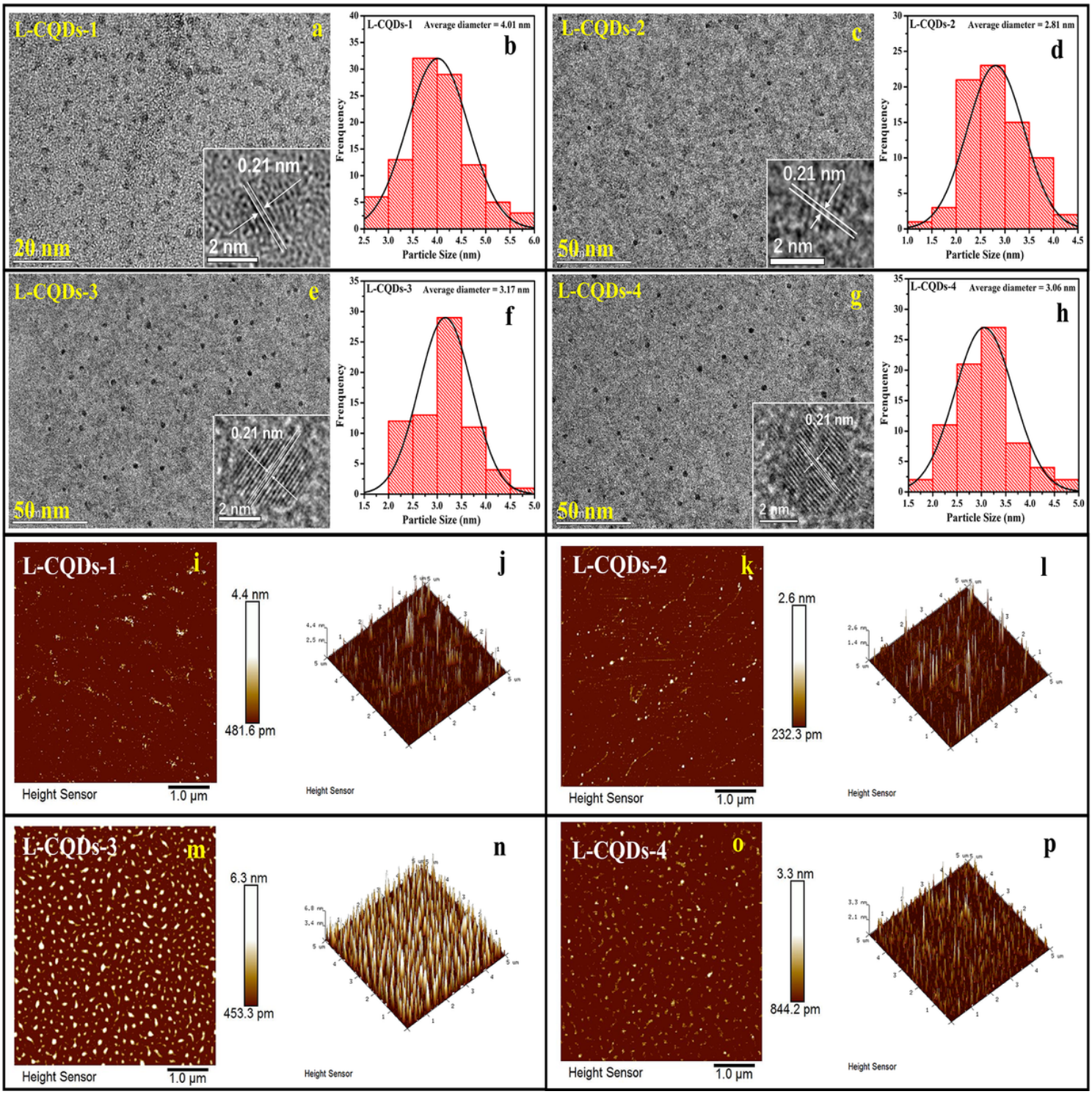

Figure 4

TEM images of (**a**) L-CQDs-1, (**c**) L-CQDs-2, (**e**) L-CQDs-3, and (**g**) L-CQDs-4, and particle size distribution of (**b**) L-CQDs-1, (**d**) L-CQDs-2, (**f**) L-CQDs-3, and (**h**) L-CQDs-4. 2D AFM images of (**i**) L-CQDs-1, (**k**) L-CQDs-2, (**m**) L-CQDs-3, and (**o**) L-CQDs-4 and 3D AFM images of (**j**) L-CQDs-1, (**l**) L-CQDs-2, (**n**) L-CQDs-3, and (**p**) L-CQDs-4. Insets in (**a, c, e, g**) show high-resolution topography.

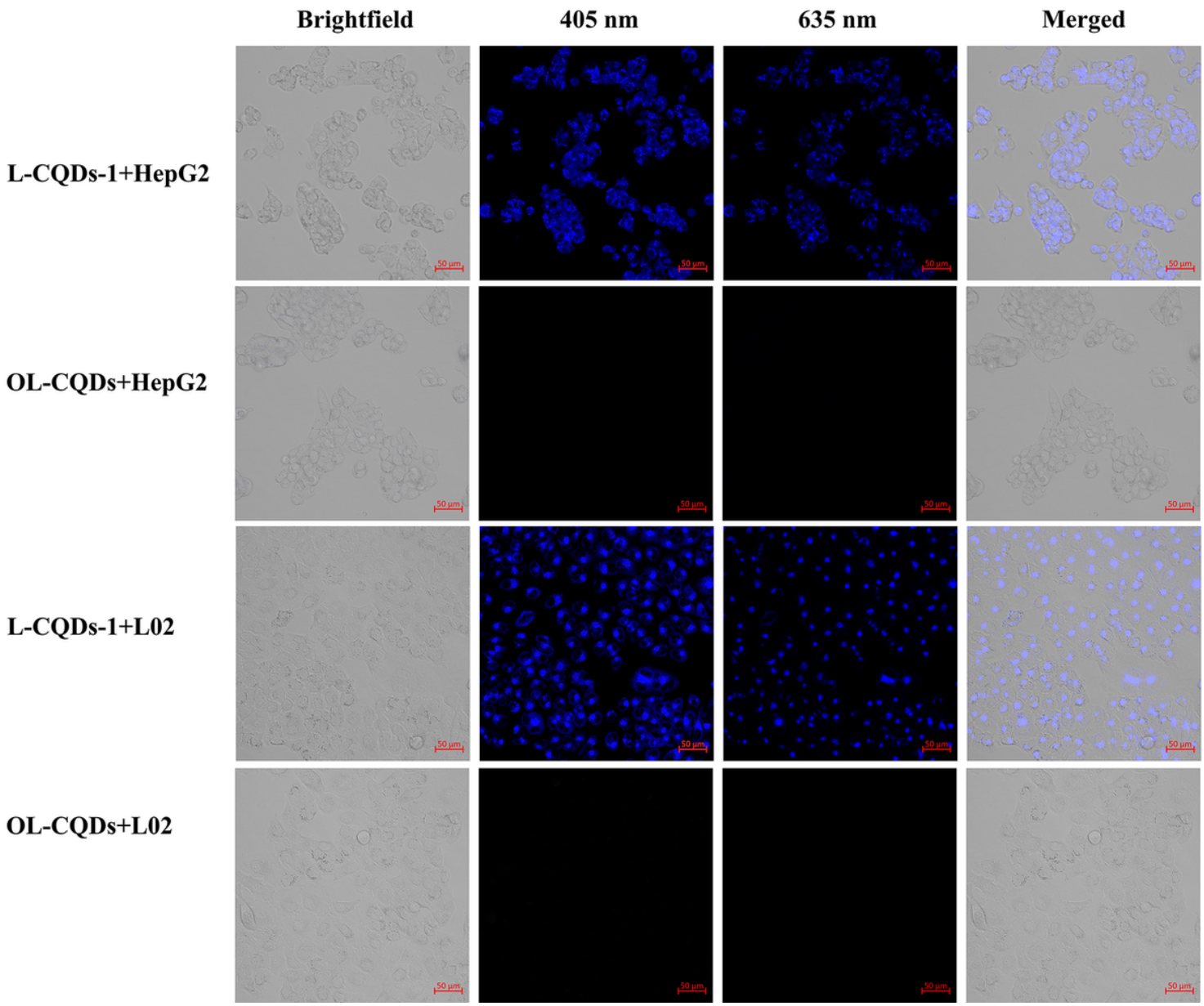

Figure 5

Brightfield images and LSCM images (λ = 405 nm and 635 nm) of HepG2 and L02 cells incubated with L-CQDs-1 and OL-CQDs for 12 h at 37 °C.

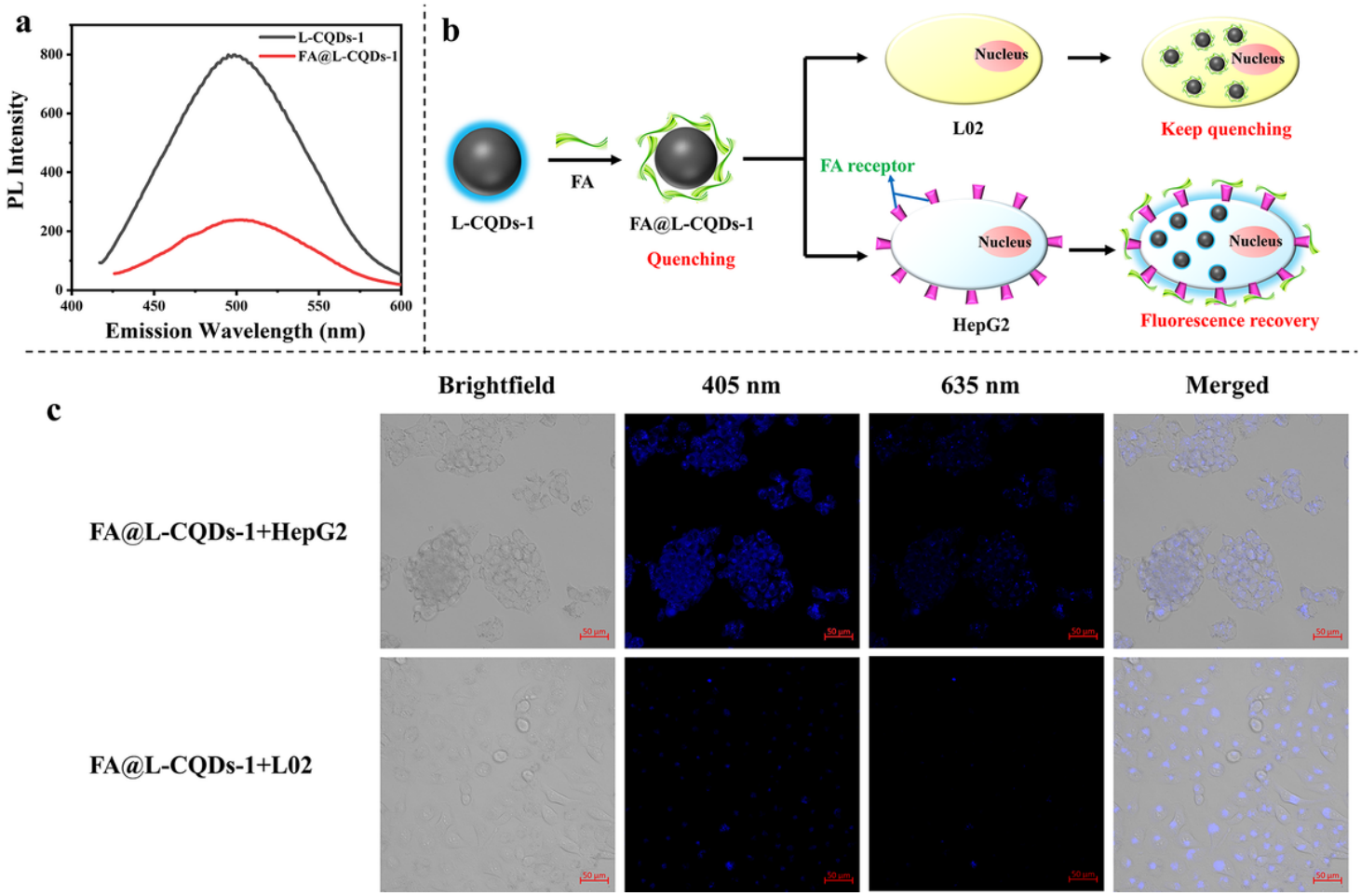

Figure 6

(**a**) Fluorescence intensity comparison of L-CQDs-1 and FA@L-CQDs-1 (λ = 405 nm), (**b**) mechanism of L-CQDs-1 targeting cancer cells, and (**c**) brightfield images and LSCM images (λ = 405 nm and 635 nm) of HepG2 and L02 cells incubated with FA@L-CQDs-1 for 12 h at 37 °C.

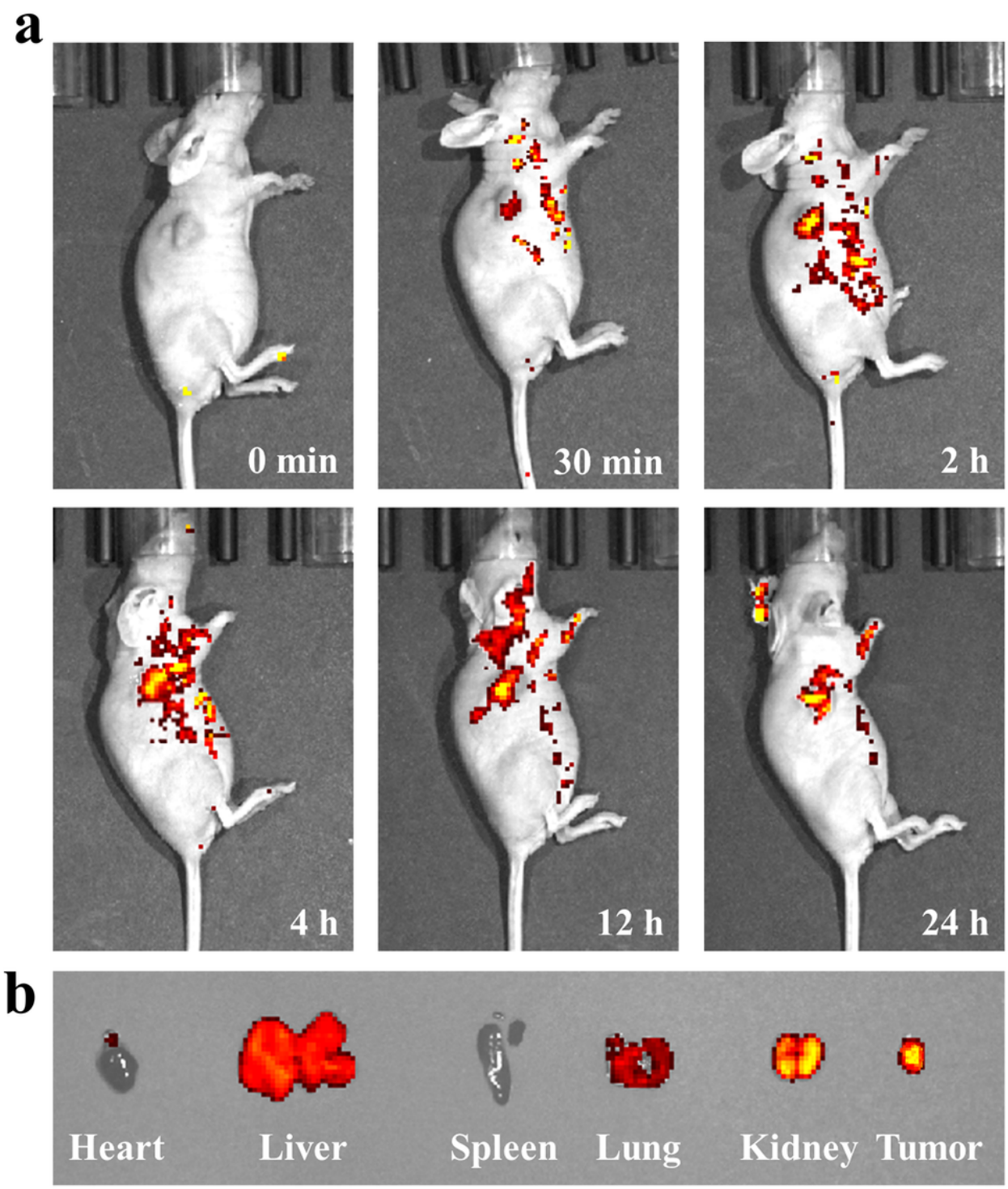

Figure 7

(**a**) In-vivo fluorescence imaging of nude mice after intravenous injection of the FA@L-CQDs-1 solution at different times (injection volume =100 μL) and (**b**) fluorescence images of the main dissected organs of nude mice after intravenous injection of the FA@L-CQDs-1 solution for 24 h.

Supplementary Files

This is a list of supplementary files associated with this preprint. Click to download.

- Scheme1.tif
- Scheme2.tif
- SupplementaryinformationACHM12.10.docx